

Insulator-to-Metal Transition at Oxide Interfaces Induced by WO₃ Overlayers

Mattoni, Giordano; Baek, David J.; Manca, Nicola; Verhagen, Nils; Groenendijk, Dirk J.; Kourkoutis, Lena F.; Filippetti, Alessio; Caviglia, Andrea D.

DOI

[10.1021/acsami.7b13202](https://doi.org/10.1021/acsami.7b13202)

Publication date

2017

Document Version

Accepted author manuscript

Published in

ACS Applied Materials and Interfaces

Citation (APA)

Mattoni, G., Baek, D. J., Manca, N., Verhagen, N., Groenendijk, D. J., Kourkoutis, L. F., Filippetti, A., & Caviglia, A. D. (2017). Insulator-to-Metal Transition at Oxide Interfaces Induced by WO₃ Overlayers. *ACS Applied Materials and Interfaces*, 9(48), 42336-42343. <https://doi.org/10.1021/acsami.7b13202>

Important note

To cite this publication, please use the final published version (if applicable).
Please check the document version above.

Copyright

Other than for strictly personal use, it is not permitted to download, forward or distribute the text or part of it, without the consent of the author(s) and/or copyright holder(s), unless the work is under an open content license such as Creative Commons.

Takedown policy

Please contact us and provide details if you believe this document breaches copyrights.
We will remove access to the work immediately and investigate your claim.

Enhancement of electron mobility at oxide interfaces induced by WO₃ overlayers

G. Mattoni,¹ D. J. Baek,² N. Manca,¹ N. Verhagen,¹ L. F. Kourkoutis,³ A. Filippetti,⁴ and A.D. Caviglia¹

¹*Kavli Institute of Nanoscience, Delft University of Technology, Netherlands*

²*School of Electrical and Computer Engineering,
Cornell University, Ithaca, New York 14853, USA*

³*School of Applied and Engineering Physics and Kavli Institute at Cornell for Nanoscale Science,
Cornell University, Ithaca, New York 14853, USA*

⁴*Dipartimento di Fisica, Universit di Cagliari, and CNR-IOM,
Istituto Officina dei Materiali, Cittadella Universitaria, Cagliari, Monserrato 09042-I, Italy*

(Dated: April 24, 2017)

Interfaces between complex oxides constitute a unique playground for 2D electron systems (2DES), where superconductivity and magnetism can arise from combinations of bulk insulators. The 2DES at the LaAlO₃/SrTiO₃ interface is one of the most studied in this regard, and its origin is determined by both the presence of a polar field in LaAlO₃ and the insurgence of point defects, such as oxygen vacancies and intermixed cations. These defects usually reside in the conduction channel and are responsible for a decreased electronic mobility. In this work, we use an amorphous WO₃ overlayer to control the defect formation and obtain an increased electron mobility in WO₃/LaAlO₃/SrTiO₃ heterostructures. The studied system shows a sharp insulator-to-metal transition as a function of both LaAlO₃ and WO₃ layer thickness. Low-temperature magnetotransport reveals a strong magnetoresistance reaching 900% at 10 T and 1.5 K, the presence of multiple conduction channels with carrier mobility up to 80 000 cm² V⁻¹ s⁻¹ and an unusually high effective mass of 5.6 m_e . The amorphous character of the WO₃ overlayer makes this a versatile approach for defect control at oxide interfaces, which could be applied to other heterostructures disregarding the constraints imposed by crystal symmetry.

The formation of a two-dimensional electron system (2DES) at the interface between band insulators SrTiO₃ (STO) and LaAlO₃ (LAO) is among the most intriguing effects studied in oxide electronics [1]. Gate tunable superconductivity [2, 3], strong spin-orbit coupling [4, 5] and magnetism [6, 7] are some of the many phenomena observed. The origin of this 2DES is a long standing question in the solid state community and recent results indicate that a consistent picture should take into account both the built-in polar field and the presence of point defects [8–10]. Among these, oxygen vacancies and cation off-stoichiometry in STO are capable of inducing a 2DES [11, 12]. However, defects residing in the conductive channel are usually responsible for a decreased electronic mobility [13]. In order to promote high electron mobility, it is crucial to confine donor sites away from the conducting plane, without preventing the 2DES formation in the STO top layers. Previous attempts to control the defect concentration profile and thus enhance the mobility involved the use of crystalline insulating overlayers [14, 15], adsorbates [16], amorphous materials [17] and even thin metallic layers [18, 19]. A promising material to control defect formation is tungsten oxide WO₃. The several possible oxidation states of tungsten make WO₃ particularly active in undergoing redox reactions. For this reason this material is often utilized in electrochemical applications and electrochromic devices [20–22]. Also, both crystalline and amorphous WO₃ can host vacancies and interstitial atoms, thus allowing cation accommodation and diffusion, with a tendency to form compounds such as tungsten bronzes [23, 24]. Recent

progress demonstrated the high-quality growth of WO₃ thin films on perovskite materials [25–27].

In this work we combine the use of a crystalline LAO/STO interface with the high reactivity of amorphous WO₃ to realise a high-mobility metallic 2DES in WO₃/LAO/STO heterostructures. Our approach is based on the tendency of WO₃ to undergo redox reactions, whose contribution is primarily manifested by the reduction of the critical LAO thickness required for the formation of a 2DES. We characterise the transport properties of this system as a function of WO₃ and LAO thickness and find multi-band conduction and an increased electron mobility up to 80 000 cm² V⁻¹ s⁻¹. The multi-band conduction leads to a remarkably strong classical magnetoresistance, which reaches 900% at 10 T and 1.5 K. Furthermore, the analysis of Shubnikov-de Haas oscillations unveils an unusually large effective mass of the highly mobile electrons.

Ultra-thin heterostructures of amorphous WO₃ and crystalline LAO are grown on TiO₂-terminated STO (001) substrates by pulsed laser deposition (details on the growth are provided in the supplementary information). We denote by (m, n) the crystalline equivalent number of unit cells (u.c.) of WO₃ and LAO, respectively, that form the heterostructure. To investigate structurally the WO₃/LAO/STO heterostructure, we perform high-angle annular dark-field scanning transmission electron microscopy (HAADF-STEM). The HAADF-STEM images in figs. 1a and 1b acquired from a (4, 2) heterostructure show uniform layers of amorphous WO₃ corresponding to 4 u.c. in thickness, followed by 2 u.c. of crystalline

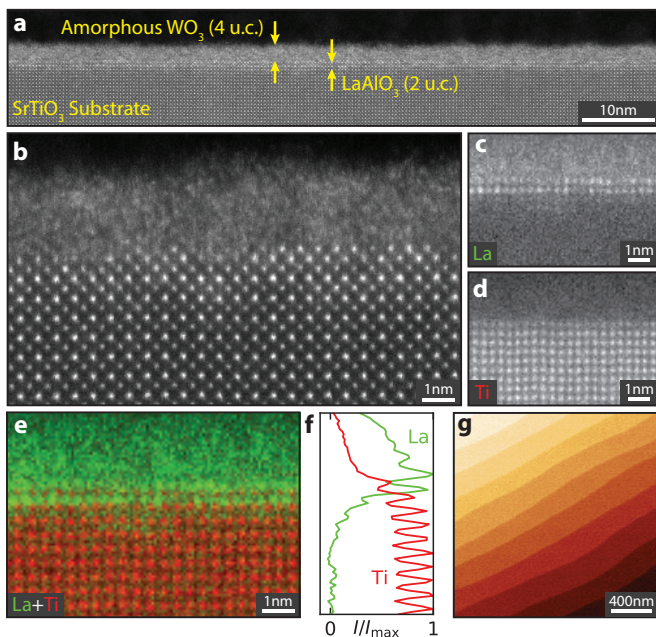


FIG. 1. **Structural characterisation of $\text{WO}_3/\text{LAO}/\text{STO}$ heterostructures.** (a) Lower magnification and (b) close-up HAADF-STEM image from a (4,2) heterostructure along the (001) direction. (c) EELS elemental map showing normalized core-loss signals for La- $M_{4,5}$, (d) Ti- $L_{2,3}$ edges and (e) combined signal. (f) Normalised EELS intensity profile averaged along the direction perpendicular to the interface. (g) Surface topography by AFM.

LAO. Due to the atomic number difference between La and Sr, the HAADF signal from the LAO is more intense than from the underlying STO substrate, as expected. To further confirm the growth of LAO, electron energy loss spectroscopy (EELS) is subsequently performed. With an energy dispersion of 0.25 eV/channel, the Ti- $L_{2,3}$ and La- $M_{4,5}$ edges are recorded simultaneously, providing atomic-resolution Ti and La elemental maps as presented in figs. 1c to 1e. By averaging the La map parallel to the interface in fig. 1f, two clear peaks are shown for La, consistent with the growth of 2 LAO layers in our heterostructure. However, significant diffusion of La into the WO_3 is also observed. The surface of all heterostructures is additionally measured by atomic force microscopy (fig. 1g), revealing the same regular steps and terraces of the underlying STO substrate, indicating uniform film growth.

The series of resistance versus temperature curves of (m, n) heterostructures in fig. 2a, shows a sharp thickness-dependent insulator-to-metal transition. The transport measurements are performed in a Van der Pauw configuration (see methods for details). For different (m, n) combinations the samples show either insulating (orange curves) or metallic (blue curves) character, with a sharp

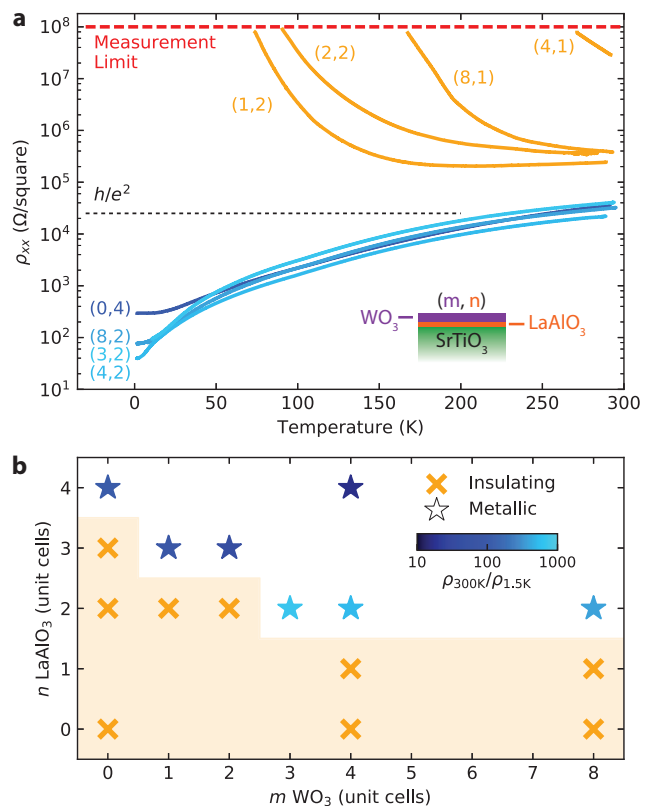


FIG. 2. **Insulator-to-metal transition in $\text{WO}_3/\text{LAO}/\text{STO}$ heterostructures.** (a) Resistance versus temperature for different (m, n) thickness combinations and (b) transport phase diagram showing insulating (orange cross) and metallic (stars with colour scale) heterostructures. The colour scale indicates the residual-resistance ratio for the metallic samples and the orange shaded area marks the (m, n) combinations constituting insulating heterostructures.

transition between the two regimes as function of layer thickness. This can be noted comparing the (4,1) and (4,2) curves, where a variation of a single u.c. of the LAO interlayer determines a three orders of magnitude resistivity difference at room temperature, which diverges upon cooling. It is noteworthy that the onset of the metallic state corresponds to the sheet resistance value h/e^2 (dotted line in fig. 2a) which is the quantum limit for metallicity in 2D [28], suggesting this electronic system has a two-dimensional nature.

The interplay between WO_3 and LAO thicknesses is summarised in the phase diagram of fig. 2b, where we indicate with a shaded orange background the (m, n) combinations resulting in insulating samples. For LAO-only films (0, n) we reproduce the well-known critical thickness for metallicity of 4 unit cells in crystalline LAO/STO interfaces, while samples with only WO_3 ($m, 0$) are always insulating. Heterostructures with 1 u.c. of LAO ($m, 1$) show an insulating state, independently of the WO_3 layer

thickness. When $n = 2$ the insulating state persists for WO_3 thickness $m \leq 2$ only, above which a metallic state is induced. With 3 cells of LAO a single layer of WO_3 is enough to trigger the metallic state. We can compare the metallicity of the conducting heterostructures by evaluating their residual resistivity ratio, defined as $\text{RRR} = \rho_{xx}(300\text{ K})/\rho_{xx}(1.5\text{ K})$. Higher RRR values indicate more pronounced metallic behaviour and are represented by the colour map in fig. 2b. Our reference LAO/STO heterostructure (0,4) has $\text{RRR} = 110$, similarly to previous reports [12, 29]. In the $\text{WO}_3/\text{LAO}/\text{STO}$ system we find higher values for decreasing thickness of the LAO interlayer. As an example, the (4,2) combination shows $\text{RRR} = 700$. A simple interpretation for this trend can be provided by considering two competing effects. On the one hand the spatially closer the amorphous WO_3 overlayer is to the STO, the more effective it is in controlling defect formation and maintaining a clean conductive channel. On the other hand a sufficiently thick LAO interlayer is required to provide the polar electric field necessary for driving charge carriers at the LAO/STO interface. The optimal balance of these two effects seems to be achieved for 2 u.c. of LAO, where we measure the highest RRR value. In this picture we are thus able to combine the mobility enhancement provided by the amorphous overlayer with the advantage of a crystalline conductive interface.

The characteristics of this metallic state are investigated by performing magnetotransport measurements on a (4,2) heterostructure, which shows a high RRR value. In fig. 3a we present its magnetoresistance (MR) which is defined as $\text{MR} = \frac{\rho_{xx}(B) - \rho_0}{\rho_0}$, where ρ_0 is the sheet resistance at $B = 0$ and the magnetic field is applied perpendicular to the interface plane. At 1.5 K the MR is positive and reaches 900% at 10 T, corresponding to one order of magnitude increase in sheet resistance. This response is very different from what is usually observed in LAO/STO heterostructures (0, n) as can be seen from the comparison with a (0,4) sample in fig. 3a. The LAO/STO, in fact, shows a positive MR of only 12% at 10 T.

The Hall resistance of the (4,2) heterostructure (fig. 3b) is negative, indicating electronic transport, with a kink at about 1 T. A non-linear component in the Hall effect is typically related to multiple conduction channels contributing to the transport. In the simplest approximation of two independent channels in parallel, the classical

magnetoresistance and the Hall resistance are given by

$$\rho_{xx} = \frac{(n_{\text{I}}\mu_{\text{I}} + n_{\text{II}}\mu_{\text{II}}) + (n_{\text{I}}\mu_{\text{II}} + n_{\text{II}}\mu_{\text{I}})\mu_{\text{I}}\mu_{\text{II}}B^2}{(n_{\text{I}}\mu_{\text{I}} + n_{\text{II}}\mu_{\text{II}})^2 + (n\mu_{\text{I}}\mu_{\text{II}}B)^2} \cdot \frac{1}{e}, \quad (1a)$$

$$\rho_{xy} = \frac{(\pm n_{\text{I}}\mu_{\text{I}}^2 \pm n_{\text{II}}\mu_{\text{II}}^2) + n(\mu_{\text{I}}\mu_{\text{II}}B)^2}{(n_{\text{I}}\mu_{\text{I}} + n_{\text{II}}\mu_{\text{II}})^2 + (n\mu_{\text{I}}\mu_{\text{II}}B)^2} \cdot \frac{B}{e}, \quad (1b)$$

where n_i , μ_i are the carrier density and mobility of the i -th channel, $n = (\pm n_{\text{I}} \pm n_{\text{II}})$ and the \pm sign indicates hole or electron carriers, respectively. We use eq. (1b) to fit with good agreement the (4,2) Hall data (dashed line in fig. 3b) and extract in table I the corresponding transport parameters (see methods for details). The (4,2) heterostructure presents two channels of electrons: one with lower-mobility $\mu_{\text{I}} = 3600\text{ cm}^2\text{ V}^{-1}\text{ s}^{-1}$, $n_{\text{I}} = 1.7 \times 10^{13}\text{ cm}^{-2}$ and one with higher mobility $\mu_{\text{II}} = 80\,000\text{ cm}^2\text{ V}^{-1}\text{ s}^{-1}$, $n_{\text{II}} = 9.3 \times 10^{12}\text{ cm}^{-2}$. Higher mobility values are observed for lower carrier densities, consistent with previous studies of STO-based 2DES [30]. We note that the sheet resistance of the higher-mobility channel ρ_{II} is one order of magnitude smaller than ρ_{I} , suggesting that it dominates the low-temperature transport. The (4,2) mobility is about two orders of mag-

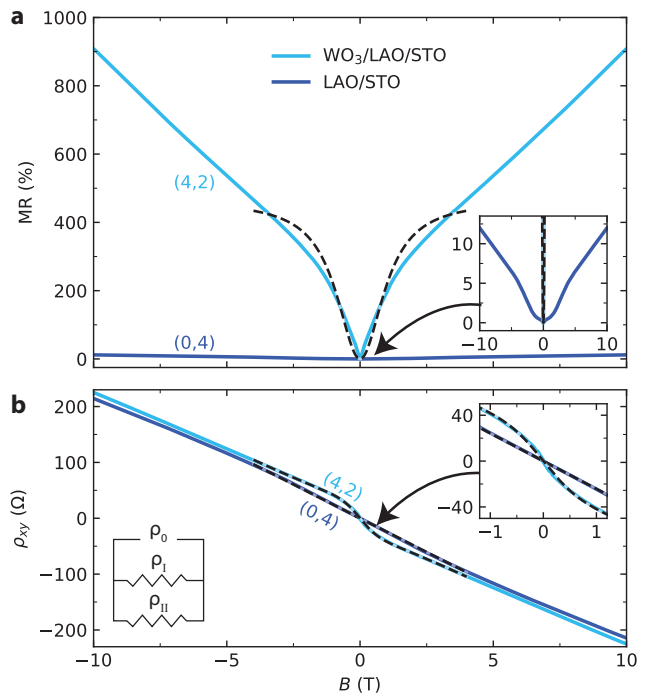


TABLE I. **Transport parameters.** Mobility, carrier density, sheet resistance and mean free path of the conductive channels extracted from the fits in fig. 3b.

| | μ ($\text{cm}^2\text{ V}^{-1}\text{ s}^{-1}$) | $n_{2\text{D}}$ (cm^{-2}) | ρ_0 (Ω) | λ (nm) |
|---------------------|---|--------------------------------------|-----------------------|----------------|
| (2,4) _{II} | 80 000 | 9.3×10^{12} | 8 | 4100 |
| (2,4) _I | 3600 | 1.7×10^{13} | 100 | 250 |
| (4,0) _I | 840 | 2.6×10^{13} | 290 | 70 |

FIG. 3. **Comparison of $\text{WO}_3/\text{LAO}/\text{STO}$ and LAO/STO magnetotransport.** (a) Magnetoresistance and (b) Hall effect measured at 1.5 K in Van der Pauw geometry, with respective zoom-in (insets). The Hall data is fitted (dashed lines) with eq. (1b) and used to extract the values in table I. The classical MR (dashed line in (a)) is calculated from these value using eq. (1a).

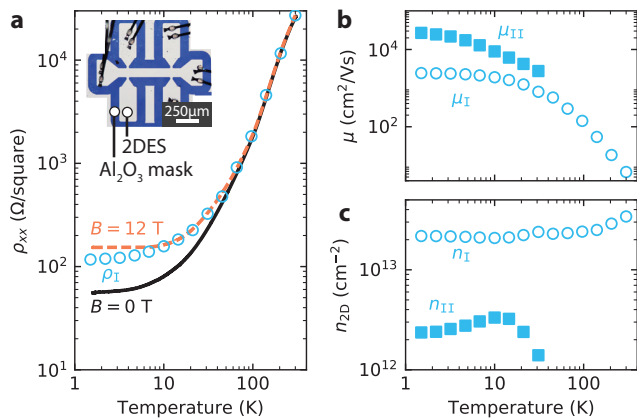


FIG. 4. **Temperature dependence of the magneto-transport.** (a) Resistance versus temperature with applied perpendicular magnetic field $B = 0$ and $B = 12$ T for a (4, 2) $\text{WO}_3/\text{LAO}/\text{STO}$ heterostructure and resistivity of the lower-mobility channel (circles). The inset shows an optical image of a $100\ \mu\text{m} \times 500\ \mu\text{m}$ Hall bar used for electrical characterisation. (b) Mobility and (c) carrier density as a function of temperature for the two channels (squares and circles) extracted from magneto-transport fits with eq. (1b).

nitude higher than what observed in the reference (0, 4) sample ($\mu_{\text{I}} = 840\ \text{cm}^2\ \text{V}^{-1}\ \text{s}^{-1}$). The absence of a higher-mobility channel is coherent with the higher resistivity at 1.5 K and the lower RRR value usually found in LAO/STO heterostructures.

Using n_i , μ_i extracted from the Hall effect we calculate with eq. (1a) the classical two-channels MR (dashed line in fig. 3a). The resulting curve accounts for a good extent of the measured signal, which is thus the dominant MR contribution, in particular for small magnetic fields. The residual MR can arise from the presence of further conduction channels or disorder (Supplementary Figure 5). Quantum corrections might also be present, but considering their typical magnitude, they are negligible compared to the other contributions.

A better insight into the effects of these parallel conduction channels is given by tracking the resistivity and Hall coefficient as a function of temperature. The measurements are performed in a $100\ \mu\text{m} \times 500\ \mu\text{m}$ Hall bar geometry (inset of fig. 4a), where the conductive regions are defined using an insulating Al_2O_3 hard mask, as described in the methods. In fig. 4a we compare the resistivity versus temperature curve measured with a magnetic field of 0 T and 12 T applied perpendicular to the interface plane. At 1.5 K the curves are well separated, underscoring a strong positive MR of 200%. On warming, the MR decreases and disappears below our measurement limit around room temperature.

By tracking the Hall effect as a function of temperature (Supplementary Figure 4) we can investigate the temperature dependence of n_i , μ_i for the different channels. A

non-linear Hall effect is observed between 1.5 K and 30 K, while a linear trend is seen at higher temperatures. The extracted mobilities and carrier densities are presented in figs. 4b and 4c. In this patterned sample we measure $\mu_{\text{I}} = 2500\ \text{cm}^2\ \text{V}^{-1}\ \text{s}^{-1}$ and $\mu_{\text{II}} = 27\ 000\ \text{cm}^2\ \text{V}^{-1}\ \text{s}^{-1}$ at 1.5 K. With increasing temperature, at first μ_{I} retains an almost constant value while μ_{II} decreases. Above 30 K the high-mobility channel disappears and the Hall effect becomes linear, signalling the cross-over to single channel transport. At higher temperatures μ_{I} decreases several orders of magnitude and reaches $\mu_{\text{I}} = 7\ \text{cm}^2/\text{Vs}$ at room temperature. This trend is similar to what has previously been reported for LAO/STO heterostructures [31].

The strong MR in our system can be explained by considering the peculiar characteristics of the two conduction channels. In general, the classical theory of MR gives a strong resistivity increase with applied magnetic field whenever the charge carriers possess high mobility. To observe high MR in systems with multiple channels it is also required that the high mobility channel is dominant in the electronic conduction (i.e. $\rho_{\text{II}}/\rho_{\text{I}} \ll 1$). Both conditions are met in our $\text{WO}_3/\text{LAO}/\text{STO}$ system, where we find a direct correlation between the ratio $\rho_{\text{II}}/\rho_{\text{I}}$ and the MR magnitude at 10 T: with $\rho_{\text{II}}/\rho_{\text{I}} \sim 10^{-1}$ in fig. 3 we measure MR $\sim 900\%$, and with $\rho_{\text{II}}/\rho_{\text{I}} \sim 1$ in fig. 4 we have a lower MR $\sim 200\%$. A further confirmation of this behaviour is given by considering that ρ_{I} values in fig. 4a well represent the resistivity versus temperature curve at $B = 12$ T. This indicates that the high-mobility channel is suppressed in the transport at high magnetic field.

The carrier density of the two conduction channels present opposite trends as a function of temperature. At 1.5 K we find that the lower-mobility channel has a higher density $n_{\text{I}} = 2.2 \times 10^{13}\ \text{cm}^{-2}$, and the higher-mobility has a lower-density $n_{\text{II}} = 2.4 \times 10^{12}\ \text{cm}^{-2}$. Upon warming, n_{I} maintains an almost constant value, while n_{II} undergoes a sharp drop above 10 K and subsequently disappears. This disappearance might be due to the activation of interband scattering processes at higher temperatures, which cause a mixing of ρ_{I} , ρ_{II} , so that their populations cannot be independently resolved in Hall effect measurements [30]. Another possible interpretation for this trend is that the two conduction channels are situated in STO at two different distances from the interface. The first channel might be spatially closer to the LAO layer, where electrons experience more defects and a stronger polar electric field, resulting in lower mobility and higher carrier density. The second channel, instead, could be further away from the interface, where a less-defected STO determines a higher electron mobility. In this picture, the depopulation of ρ_{II} might be linked to the drop of the STO dielectric constant upon warming [32] (Supplementary Fig. 6).

The electronic state confined in our $\text{WO}_3/\text{LAO}/\text{STO}$ heterostructures shows Shubnikov-de Haas (SdH) oscilla-

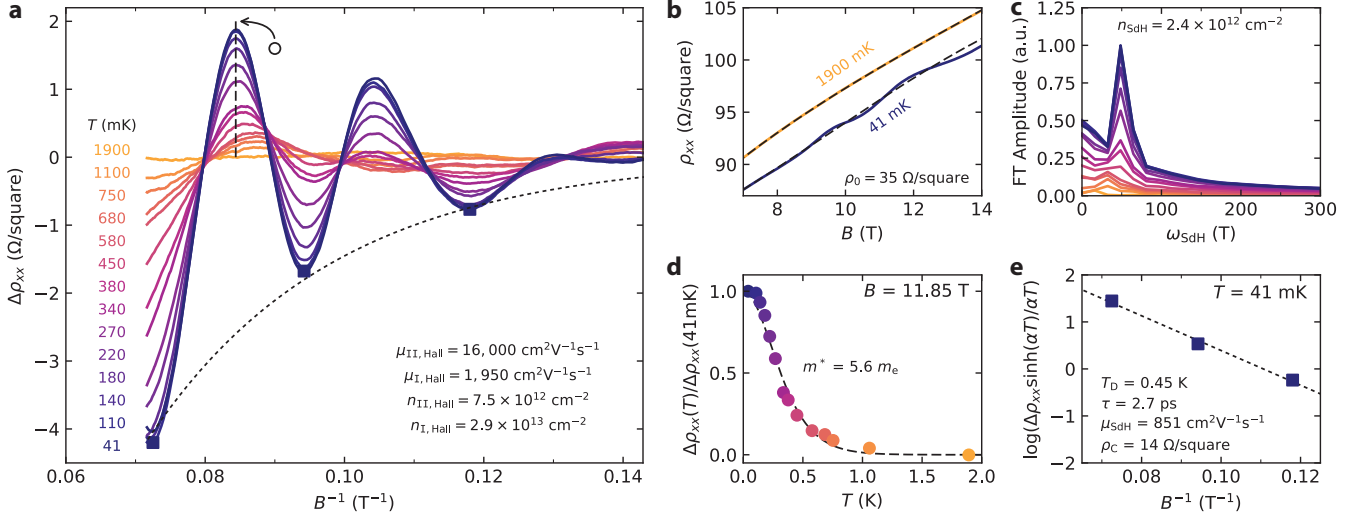


FIG. 5. **Quantum oscillations of conductance.** (a) Temperature dependence of the SdH oscillations after the removal of a 3rd order polynomial background. The dashed and dotted lines indicate the data in (d) and (e), respectively. (b) Raw ρ_{xx} data at two different temperatures showing the fit of the polynomial background (dashed lines). (c) Fourier spectra of the oscillations in the range 7 T to 14 T. (d) Temperature dependence of the oscillations amplitude at $B = 11.85$ T and fit to eq. (2) (dashed line) from which the carrier effective mass m^* is extracted. (e) Dingle plot of the SdH oscillations minima at $T = 41$ mK and fit to eq. (2) (dotted line) from which the Dingle temperature T_D , elastic scattering time τ , mobility μ_{SdH} and the classical sheet resistance ρ_c are extracted.

tions superimposed on the background of strong positive MR. The SdH as a function of temperature are shown in fig. 5a, where their signal was extracted by fitting the background with a 3rd order polynomial (dashed line in fig. 5b). The oscillations disappear when the magnetic field is applied parallel to the interface plane, as expected for a two-dimensional system. SdH oscillations in 2DES can be modelled by

$$\Delta\rho_{xx} = 4\rho_c e^{-\alpha T_D} \frac{\alpha T}{\sinh(\alpha T)} \sin\left(2\pi \frac{\omega_{\text{SdH}}}{B}\right), \quad (2)$$

where ρ_c is the classical sheet resistance in zero magnetic field, $\alpha = 2\pi^2 k_B / \hbar \omega_c$ with cyclotron frequency $\omega_c = eB/m^*$, Boltzmann's constant k_B , reduced Planck's constant \hbar , carrier effective mass m^* and Dingle temperature T_D . Fourier analysis in fig. 5c reveals that the oscillations are periodic in B^{-1} , with a single frequency peak at $\omega_{\text{SdH}} = 49$ T. Assuming a 2DES with circular sections of the Fermi surface, we can estimate the carrier density as $n_{\text{SdH}} = \omega_{\text{SdH}} \nu_s e / h$, where ν_s indicates the spin degeneracy. By considering $\nu_s = 2$ we find $n_{\text{SdH}} = 2.4 \times 10^{12} \text{ cm}^{-2}$. We note that even if Hall effect measurements indicate the presence of two conduction channels (values in fig. 5a), only one channel contributes to the quantum oscillations. Furthermore, the obtained n_{SdH} is lower than both n_{II} , n_{I} for this sample, so that it is not possible to associate the SdH oscillation to one specific channel. A discrepancy between n_{SdH} and n_{Hall} in LAO/STO interfaces has already been reported and

its origin remains unknown [33, 34].

To extract the mass of the electrons showing the SdH effect, in fig. 5d we track the oscillation amplitude at $B = 11.85$ T as a function of temperature (similar results are obtained using different values of B). Fitting the trend with eq. (2), we find a surprisingly high value $m^* = 5.6 m_e$. Considering the enhanced mobility of carriers in the $\text{WO}_3/\text{LAO}/\text{STO}$ system, in fact, one would expect a decreased effective mass, while in this case m^* is three times larger than typical observations in LAO/STO heterostructures [17, 35].

A possible explanation of this electron mass renormalization can be lead back to strong electron-phonon coupling, which is enhanced by the tight spatial confinement of the 2DEG. Such coupling was previously found to produce large phonon-drag [36, 37] and polaronic effects in both LAO/STO interfaces and amorphous WO_3 thin films [38, 39]. Another possibility is that the modified defect profile with respect to conventional LAO/STO interfaces determines a mass enhancement of the 2DES bands [40].

Finally, from the Dingle plot in fig. 5e we extract $T_D = 0.45$ K. This value points to an ordered electronic system with sharp Landau levels, considering that their energy smearing $k_B T_D \sim 40 \mu\text{eV}$ is much smaller than their spacing $\hbar \omega_C \sim 250 \mu\text{eV}$. The extracted value $\rho_c = 14 \Omega/\text{square}$ is in good agreement with $\rho_0 = 35 \Omega/\text{square}$, corroborating the performed analysis. Using $T_D = \hbar / 2\pi k_B \tau$ and $\tau = m^* \mu_{\text{SdH}} / e$ we calculate the

elastic scattering time $\tau = 2.7$ ps and the quantum mobility $\mu_{\text{SDH}} = 851 \text{ cm}^2 \text{ V}^{-1} \text{ s}^{-1}$. Even though μ_{SDH} is lower than both the Hall effect values μ_{II} , μ_{I} , it further confirms the formation of a high mobility 2DES in the $\text{WO}_3/\text{LAO}/\text{STO}$ heterostructure.

To conclude, we have demonstrated that amorphous WO_3 is an effective overlayer to form 2DES with enhanced mobility and effective mass at LAO/STO interfaces. Reducing the crystalline LAO critical thickness from 4 to 2 unit cells, the WO_3 overlayer determined a metallic system with high RRR and increased electron mobility. We ascribed the insurgence of a strong classical magnetoresistance to the peculiar characteristics of the multiple conduction channels observed in the system. Quantum oscillations of conductance confirmed the realisation of high-quality $\text{WO}_3/\text{LAO}/\text{STO}$ heterostructures, where a strong two-dimensional confinement of carriers is achieved. All these results are achieved using an amorphous WO_3 overlayer, which does not require crystal matching. Our work thus demonstrates a new approach for defect control at oxide interfaces, which can be exploited to induce high-mobility 2DES in a broad variety of oxide materials.

EXPERIMENTAL SECTION

Samples growth: $\text{WO}_3/\text{LaAlO}_3/\text{SrTiO}_3$ heterostructures were grown by pulsed laser deposition on commercially available $5 \text{ mm} \times 5 \text{ mm}$ SrTiO_3 (001) substrates, with TiO_2 surface termination. The laser ablation was performed using a KrF excimer laser (Coherent COMPexPro 205, $\lambda = 248 \text{ nm}$) with a 1 Hz repetition rate and 1 J cm^{-2} fluence. The target-substrate distance was fixed at 55 mm. For the LaAlO_3 thin films a crystalline target was employed and the deposition performed at 800°C substrate temperature and 3×10^{-5} mbar oxygen pressure. LaAlO_3 film thickness was monitored *in-situ* during growth by intensity oscillations of reflection high-energy electron diffraction (RHEED). The samples were annealed for 1 h at 600°C in 300 mbar of O_2 atmosphere to compensate for the possible formation of oxygen vacancies. The amorphous WO_3 thin films were deposited from a WO_3 sintered target at 500°C substrate temperature and 5×10^{-3} mbar oxygen pressure. WO_3 film thickness was calibrated by depositing crystalline WO_3 on SrTiO_3 and monitoring the growth by RHEED. The thickness value was then confirmed by X-ray diffraction and transmission electron microscopy measurements (results to be published elsewhere). At the end of the growth the heterostructures were cooled down to ambient temperature in 5×10^{-3} mbar oxygen pressure (further details in Supplementary Figure 1).

Hall bar geometry fabrication: SrTiO_3 substrates were patterned prior to $\text{WO}_3/\text{LaAlO}_3$ thin films deposition with standard e-beam lithography followed by the evaporation of an insulating Al_2O_3 mask. The mask was deposited at room temperature by RF sputtering in a 5 μbar Ar atmosphere, resulting in amorphous alumina.

Electrical measurements: The measurements in figs. 2 and 3 were carried out in van der Pauw configuration, while for the ones in figs. 4 and 5 a Hall bar geometry was used. In

both measurement configurations the metallic interface was directly contacted by ultrasonically wire-bonded Al.

Non-linear Hall effect fits: The fits are performed with the least squared method using data in the magnetic field range -4 T to 4 T . The constraint $1/\rho_0 = 1/\rho_{\text{I}} + 1/\rho_{\text{II}}$ is applied to the fitting parameters, and ρ_0 is extracted from the $\rho_{xx}(B)$ measurement. With the assumption $1/\rho_i = n_i e \mu_i$, only three free parameters among ρ_i , n_i , μ_i , with $i = \text{I, II}$, are varied in the fitting procedure.

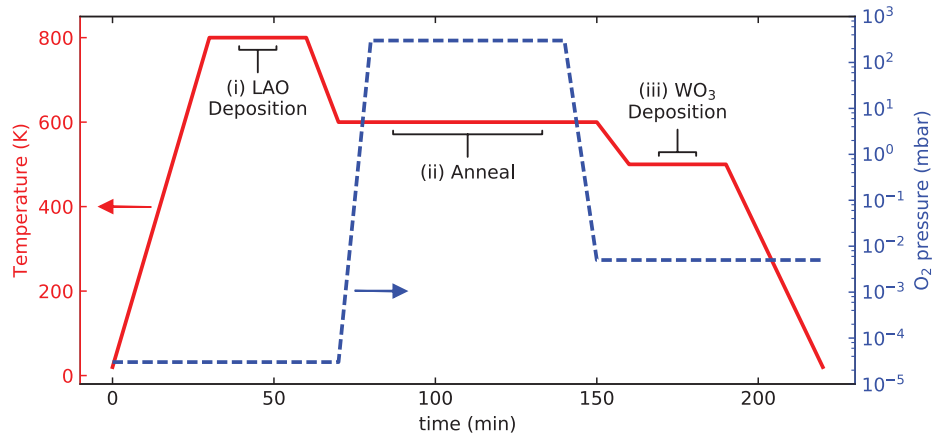
ACKNOWLEDGMENTS

We thank P. Zubko for valuable feedback and for performing XRD measurements; Y. M. Blanter and D. J. Groenendijk for fruitful discussions. This work was supported by The Netherlands Organisation for Scientific Research (NWO/OCW) as part of the Frontiers of Nanoscience program (NanoFront), the Dutch Foundation for Fundamental Research on Matter (FOM), the European Research Council under the European Union's H2020 programme/ ERC Grant Agreement n. [677458] and the Cornell Center for Materials Research with funding from the NSF MRSEC program (DMR-1120296). The FEI Titan Themis 300 TEM was acquired through NSF-MRI-1429155, with additional support from Cornell University, the Weill Institute and the Kavli Institute at Cornell. A. F. thanks TU Delft and Kavli Institute for the access to Computing Center resources, and computational support from the CRS4 Computing Center (Piscina Manna, Pula, Italy).

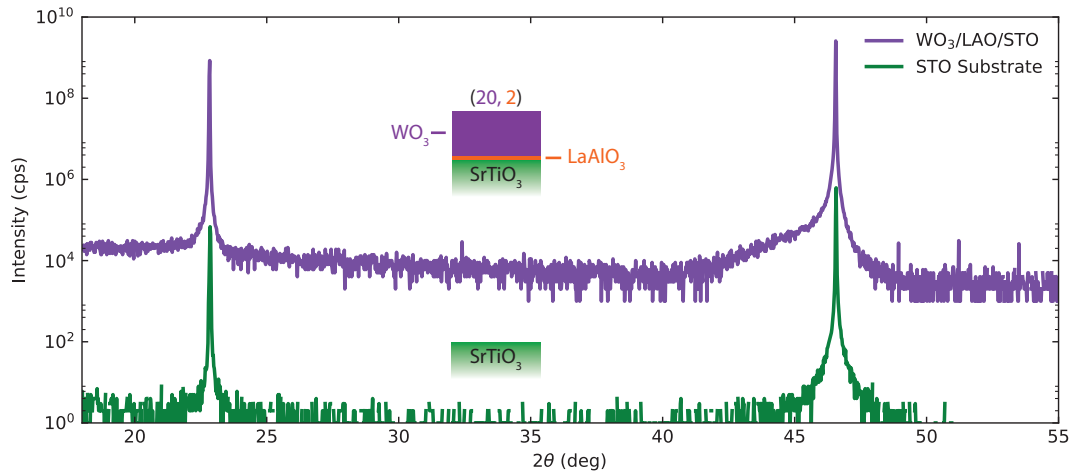
-
- [1] A. Ohtomo and H. Hwang, *Nature* **427**, 423 (2004).
 - [2] N. Reyren, S. Thiel, A. Caviglia, L. F. Kourkoutis, G. Hammerl, C. Richter, C. Schneider, T. Kopp, A.-S. Rüetschi, D. Jaccard, *et al.*, *Science* **317**, 1196 (2007).
 - [3] A. Caviglia, S. Gariglio, N. Reyren, D. Jaccard, T. Schneider, M. Gabay, S. Thiel, G. Hammerl, J. Mannhart, and J.-M. Triscone, *Nature* **456**, 624 (2008).
 - [4] A. Caviglia, M. Gabay, S. Gariglio, N. Reyren, C. Cancellieri, and J.-M. Triscone, *Physical review letters* **104**, 126803 (2010).
 - [5] M. Diez, A. Monteiro, G. Mattoni, E. Cobanera, T. Hyart, E. Mulazimoglu, N. Bovenzi, C. Beenakker, and A. Caviglia, *Physical review letters* **115**, 016803 (2015).
 - [6] J. A. Bert, B. Kalisky, C. Bell, M. Kim, Y. Hikita, H. Y. Hwang, and K. A. Moler, *Nature physics* **7**, 767 (2011).
 - [7] L. Li, C. Richter, J. Mannhart, and R. Ashoori, *Nature Physics* **7**, 762 (2011).
 - [8] N. Nakagawa, H. Y. Hwang, and D. A. Muller, *Nature materials* **5**, 204 (2006).
 - [9] F. Gunkel, P. Brinks, S. Hoffmann-Eifert, R. Dittmann, M. Huijben, J. Kleibeuker, G. Koster, G. Rijnders, and R. Waser, *Applied physics letters* **100**, 052103 (2012).

- [10] L. Yu and A. Zunger, *Nature communications* **5** (2014).
- [11] A. Kalabukhov, R. Gunnarsson, J. Börjesson, E. Olsson, T. Claeson, and D. Winkler, *Physical Review B* **75**, 121404 (2007).
- [12] M. Warusawithana, C. Richter, J. Mundy, P. Roy, J. Ludwig, S. Paetel, T. Heeg, A. Pawlicki, L. Kourkoutis, M. Zheng, *et al.*, *Nature communications* **4** (2013).
- [13] N. Bristowe, P. Littlewood, and E. Artacho, *Physical Review B* **83**, 205405 (2011).
- [14] M. Huijben, G. Koster, M. K. Kruijze, S. Wenderich, J. Verbeeck, S. Bals, E. Slooten, B. Shi, H. J. Molegraaf, J. E. Kleibeuker, *et al.*, *Advanced functional materials* **23**, 5240 (2013).
- [15] Y. Chen, F. Trier, T. Wijnands, R. Green, N. Gauquelin, R. Egoavil, D. V. Christensen, G. Koster, M. Huijben, N. Bovet, *et al.*, *Nature materials* **14**, 801 (2015).
- [16] Y. Xie, C. Bell, Y. Hikita, S. Harashima, and H. Y. Hwang, *Advanced Materials* **25**, 4735 (2013).
- [17] Y. Chen, N. Bovet, F. Trier, D. Christensen, F. Qu, N. H. Andersen, T. Kasama, W. Zhang, R. Giraud, J. Du-fouleur, *et al.*, *Nature communications* **4**, 1371 (2013).
- [18] S. Wu, X. Luo, S. Turner, H. Peng, W. Lin, J. Ding, A. David, B. Wang, G. Van Tendeloo, J. Wang, *et al.*, *Physical Review X* **3**, 041027 (2013).
- [19] E. Lesne, N. Reyren, D. Doennig, R. Mattana, H. Jaffrès, V. Cros, F. Petroff, F. Choueikani, P. Ohresser, R. Pentcheva, *et al.*, *Nature communications* **5** (2014).
- [20] S. K. Deb, *Solar Energy Materials and Solar Cells* **92**, 245 (2008).
- [21] X. Meng, F. Quenneville, F. Venne, E. Di Mauro, D. Isik, M. Barbosa, Y. Drolet, M. M. Natile, D. Rochefort, F. Soavi, *et al.*, *The Journal of Physical Chemistry C* **119**, 21732 (2015).
- [22] S. Cong, F. Geng, and Z. Zhao, *Advanced Materials* **28**, 10518 (2016).
- [23] M. Arab, A. L. Lopes-Moriyama, T. R. dos Santos, C. P. de Souza, J. R. Gavarri, and C. Leroux, *Catalysis Today* **208**, 35 (2013).
- [24] Y. He, M. Gu, H. Xiao, L. Luo, Y. Shao, F. Gao, Y. Du, S. X. Mao, and C. Wang, *Angewandte Chemie International Edition* **55**, 6244 (2016).
- [25] Y. Du, M. Gu, T. Varga, C. Wang, M. E. Bowden, and S. A. Chambers, *ACS applied materials & interfaces* **6**, 14253 (2014).
- [26] X. Leng, J. Pereiro, J. Strle, A. Bollinger, and I. Božović, *APL Materials* **3**, 096102 (2015).
- [27] S. G. Altendorf, J. Jeong, D. Passarello, N. B. Aetukuri, M. G. Samant, and S. S. Parkin, *Advanced Materials* (2016).
- [28] N. F. Mott, *International Reviews in Physical Chemistry* **4**, 1 (1985), <http://dx.doi.org/10.1080/01442358509353351>.
- [29] S. Gariglio, N. Reyren, A. Caviglia, and J. Triscone, *Journal of Physics: Condensed Matter* **21**, 164213 (2009).
- [30] F. Gunkel, C. Bell, H. Inoue, B. Kim, A. G. Swart, T. A. Merz, Y. Hikita, S. Harashima, H. K. Sato, M. Minohara, *et al.*, *Physical Review X* **6**, 031035 (2016).
- [31] A. Fête, C. Cancellieri, D. Li, D. Stornaiuolo, A. Caviglia, S. Gariglio, and J.-M. Triscone, *Applied Physics Letters* **106**, 051604 (2015).
- [32] T. Sakudo and H. Unoki, *Physical review letters* **26**, 851 (1971).
- [33] A. Caviglia, S. Gariglio, C. Cancellieri, B. Sacepe, A. Fete, N. Reyren, M. Gabay, A. Morpurgo, and J.-M. Triscone, *Physical review letters* **105**, 236802 (2010).
- [34] M. B. Shalom, A. Ron, A. Palevski, and Y. Dagan, *Physical review letters* **105**, 206401 (2010).
- [35] A. McCollam, S. Wenderich, M. Kruijze, V. Guduru, H. Molegraaf, M. Huijben, G. Koster, D. Blank, G. Rijnders, A. Brinkman, *et al.*, *APL materials* **2**, 022102 (2014).
- [36] I. Pallecchi, F. Telesio, D. Li, A. Fête, S. Gariglio, J.-M. Triscone, A. Filippetti, P. Delugas, V. Fiorentini, and D. Marré, *Nature communications* **6** (2015).
- [37] I. Pallecchi, F. Telesio, D. Marré, D. Li, S. Gariglio, J.-M. Triscone, and A. Filippetti, *Physical Review B* **93**, 195309 (2016).
- [38] C. Cancellieri, A. Mishchenko, U. Aschauer, A. Filippetti, C. Faber, O. Barišić, V. Rogalev, T. Schmitt, N. Nagaosa, and V. Strocov, *Nature communications* **7** (2016).
- [39] L. Berggren, A. Azens, and G. A. Niklasson, *Journal of Applied Physics* **90**, 1860 (2001).
- [40] W. Wunderlich, H. Ohta, and K. Koumoto, *Physica B: Condensed Matter* **404**, 2202 (2009).

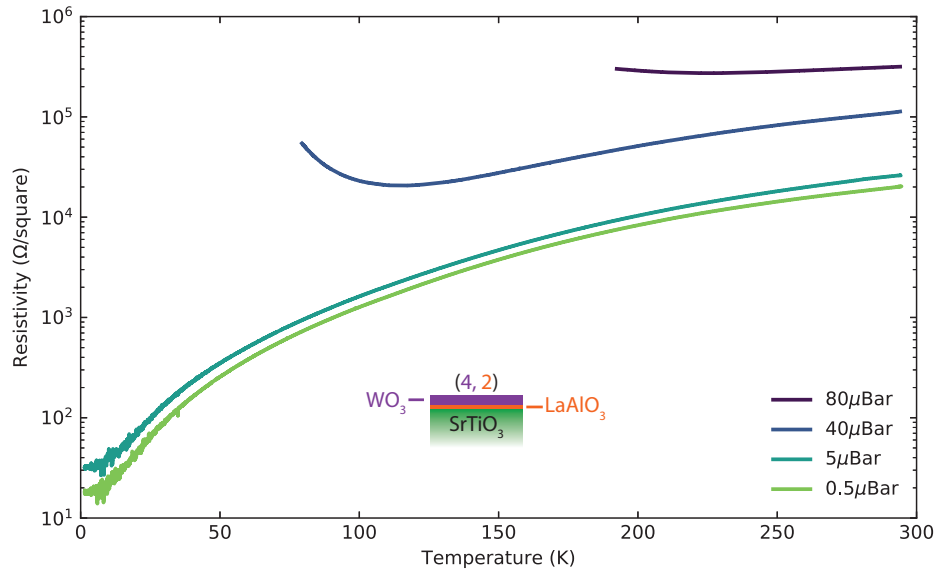
Supplementary Information



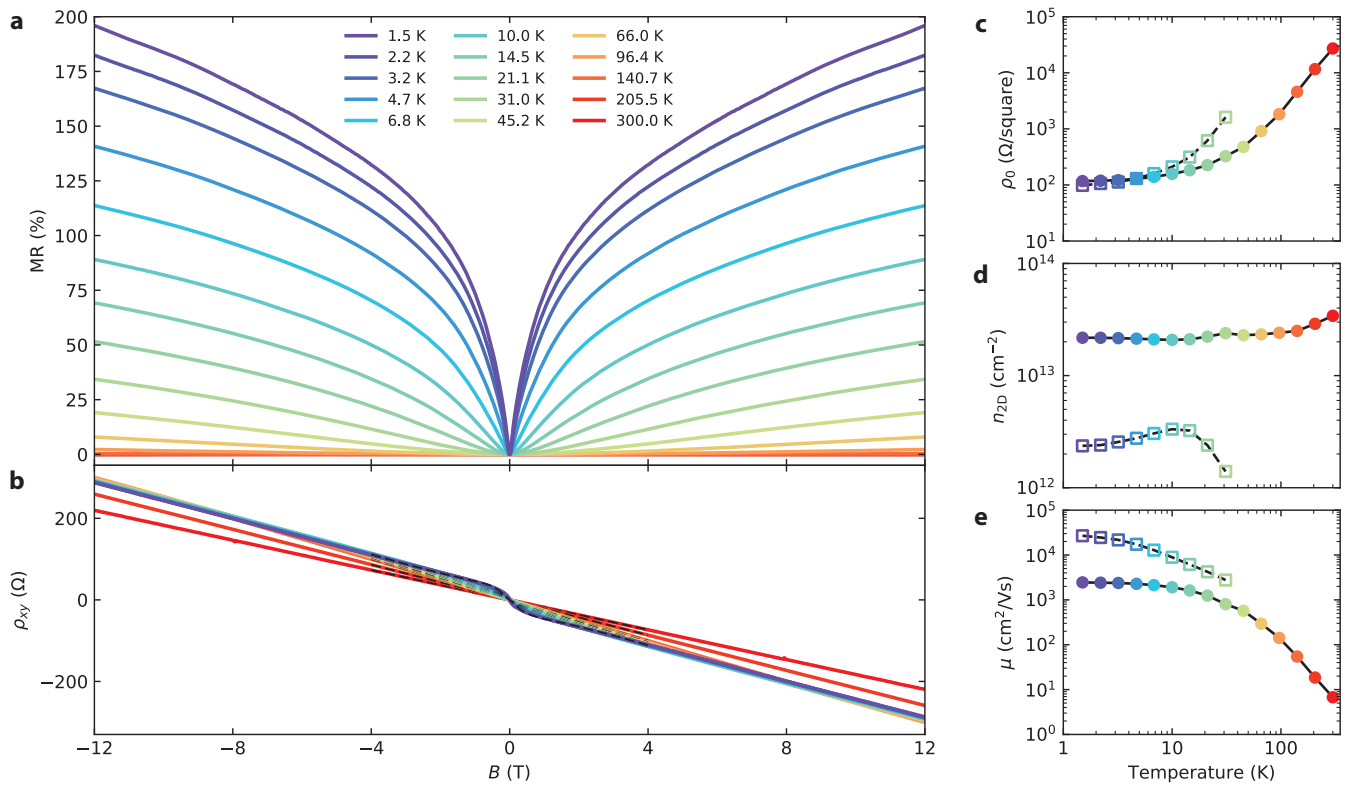
Supplementary Figure 1. **Growth conditions schematics.** Cycle of sample temperature and oxygen pressure used for the growth of all the (m, n) heterostructures: (i) heating to 800 °C in 5×10^{-4} mbar followed by possible LaAlO₃ deposition, (ii) post-growth anneal step for 1 h at 600 °C and 300 mbar, (iii) cool-down to 500 °C and 5×10^{-3} mbar followed by possible WO₃ deposition, final cool-down to room temperature. A rate of 20 °C min⁻¹ was used for all temperature ramps. The $(m, 0)$ and $(0, n)$ samples underwent the same T, p cycle, where the LAO or WO₃ deposition steps were substituted by an idling stage of a few minutes.



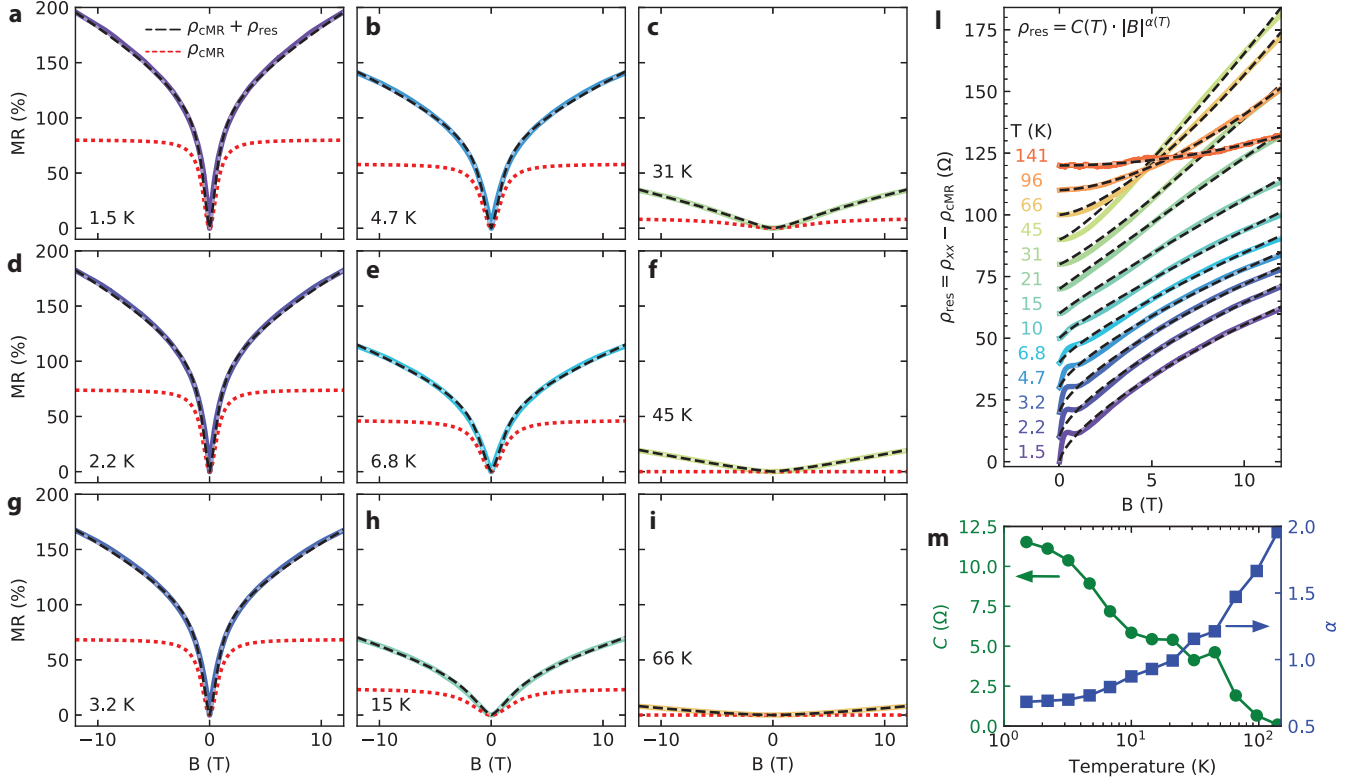
Supplementary Figure 2. **XRD comparison of an STO substrate and a $(20, 2)$ WO₃/LAO/STO heterostructure.** The $\theta - 2\theta$ X-ray diffraction scan around the (001) and (002) substrate peak shows no clear diffraction peak coming from the heterostructure, further confirming the amorphous nature of our WO₃ overlayer.

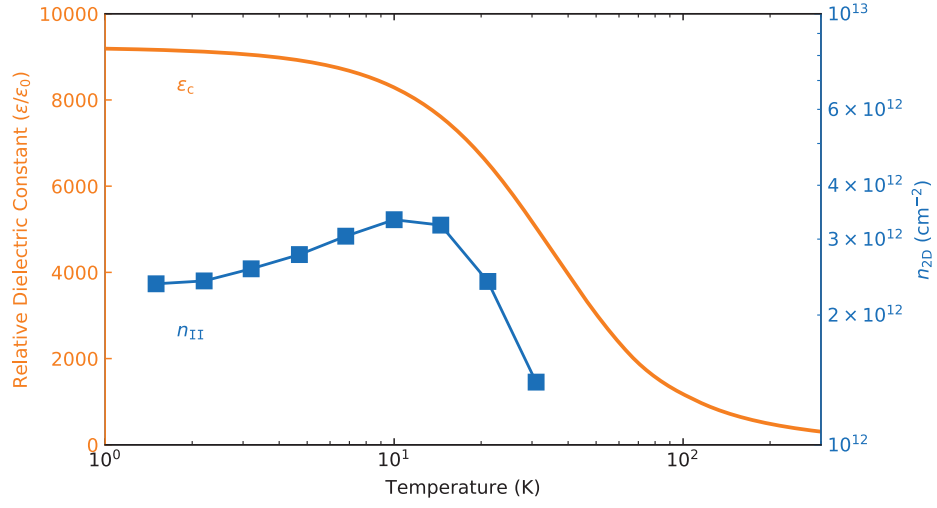


Supplementary Figure 3. **Transport of a (4, 2) WO₃/LAO/STO heterostructures where WO₃ is grown in different oxygen pressures.** We measure the metallic trend discussed in the paper only when the WO₃ overlayer is grown in a low oxygen pressure ($p_{O_2} < 40 \mu\text{bar}$). This shows the important role of defect formation, such as oxygen vacancies, in the WO₃ overlayer in order to obtain the enhanced 2DES at WO₃/LAO/STO heterostructures.



Supplementary Figure 4. **Temperature dependent magnetotransport of a (4, 2) $\text{WO}_3/\text{LAO}/\text{STO}$ heterostructure.** (a) Magnetoresistance and (b) Hall effect measured at different temperatures in a Hall bar configuration. Fits of the Hall effect curves allow to extract (c) sheet resistance, (d) carrier density and (e) mobility of the multiple conduction channels.





Supplementary Figure 6. **Comparison of STO dielectric constant with high-mobility carrier density.** Temperature dependence of the c -axis relative dielectric constant of STO (orange) from [Sakudo T. et al., PRL (1971)] and carrier density of the high mobility channel of the (4, 2) $\text{WO}_3/\text{LAO}/\text{STO}$ heterostructure in fig. 4d. We note how n_{II} decreases dramatically and then disappears in the same temperature range where the STO dielectric constant drops, suggesting the loss of high-mobility carriers can be related to a change in the STO dielectric environment.